Highly spatially resolved chemical metrology on latent resist images

Maarten van Es

Netherlands Organisation for Applied Scientific Research

Mehmet Tamer

TNO

Robbert Bloem

TNO

Laurent Fillinger

TNO

Elfi van Zeijl

TNO

Klára Maturová

TNO

Jacques van der Donck

TNO

Rob Willekers

TNO

Diederik Maas (✉ diederik.maas@tno.nl)

TNO   https://orcid.org/0000-0003-3667-3533

Research Article

Highly spatially resolved chemical metrology on latent resist images

Maarten van Es*, Selman Tamer, Elin Bloem, Laurent Fillinger, Elfi van Zeijl, Klára Maturová, Jacques van der Donck, Rob Willekers and Diederik Maas*.

Netherlands Organisation for Applied Scientific Research (TNO), Delft, Netherlands

Abstract

Patterning photoresist with extreme control over dose and placement is the first crucial step in semiconductor manufacturing. However, how can the activation of modern complex resist components be accurately measured at sufficient spatial resolution? No exposed nanometre-scale resist pattern is sufficiently sturdy to unaltered withstand inspection by intense photon or electron beams, not even after processing and development.

This paper presents experimental proof that infrared atomic force microscopy (IR-AFM) is sufficiently sensitive and gentle to chemically record vulnerable yet valuable lithographic patterns in a chemically amplified resist *after* exposure *prior* to development. Accordingly, IR-AFM metrology provides long-sought insights into changes in the chemical and spatial distribution per component in a latent resist image, both directly after exposure and during processing. With these to-be-gained understandings, a disruptive acceleration of resist design and processing is expected.

Introduction

To support the global trend of further shrinkage of transistors, satisfactory pattern fidelity in the photoresist at the nanometre scale is needed (1) (2). After lithographic patterning, resist processing is the next crucial step in semiconductor manufacturing. By processing, the vulnerable latent pattern is translated, via a more sturdy form in the developed resist, into the target wafer by e.g. etching or ion implantation (3). Resist processing requires extremely sophisticated know-how and control to optimally and reproducibly transfer (feature size) or suppress (variation of feature size), especially the high-spatial frequencies from the latent pattern via processed resist into the substrate. Since the economic value of lithography can only be harvested after defect-free pattern transfer into silicon, tight control over resist processing is of key importance. Recently, metrology by AFM has been demonstrated for 16 nm half-pitch lines on processed and developed resist (4) and 26 nm posts (5). Ideally, similar metrology would be made available to quantify the pattern development per step, i.e. after postexposure bake, develop and rinse, thus providing insight into which step is the most critical bottleneck (6). However, currently, no commercial method exists that can resolve control parameters such as critical dimension (CD) or line edge roughness (LER) in latent or partially processed resist patterns. This paper introduces a metrology method that provides insight into changes in photoresist during processing, which hitherto were not observable at the nanometre scale, without inflicting damage to or shrinkage of the exposed resist.

The semiconductor industry has developed a very sophisticated infrastructure and way of working to establish high-volume manufacturing of semiconductor circuits with deep submicron dimensions, as reported by, e.g., (7), (8) (9) (10). These sources all emphasize that LER control is critical for manufacturing, as excessive LER correlates with yield loss (11). Such will amplify for sub-10 nm patterning, as the industry foresees the need for control over the stochastics of the lithographic (EUV) image as well as the granular components of photoresist (12). Modern photoresists are

42 complex mixtures in which each component has a specific function to yield a sensitive resist that can
43 capture high-resolution images with a low roughness of the patterns (13), (14) (15) (16) (17) (18)
44 (10). Gallatin's landmark paper pointed out that a trade-off between resolution (R), uniformity (L)
45 and sensitivity (S) exists (19). Wallow translated this insight into a first widely accepted metric for a
46 CAR's performance, the Z-factor, which quantifies the area of the *RLS* triangle (20). In response,
47 industry standardised LER metrology to establish a globally uniform comparison between resist
48 performance (21). However, unravelling the chemistry in resists during processing remains a major
49 scientific challenge (22) (23) (24). In addition, industry kept looking for additional metrology
50 techniques to reduce the measurement error (25) (26) (27) (28) (29) (30) (31) (4). Further work
51 identified and quantified the impact of (blur by, e.g., shot noise in) the exposure tool image on the Z-
52 factor (32) (33) (34) (35) (36) (37) (38), which led to the introduction of k_4 as the latest resist metric
53 (39). Following the proposed protocol, it is now possible to separate the contribution to the
54 nonuniformity by shot noise in the exposed image on the one hand from the stochastic variations in
55 the resist and processing on the other hand. Nevertheless, accurate metrology for resolution and
56 uniformity is required for a reliable evaluation of both the *Z-* and *k_4*-factors.

57 As outlined in a recent LER metrology review paper by Cutler et al., there is additional unique
58 information on a photoresist's qualities disclosed in the power spectral density (PSD) of all spatial
59 frequencies that contribute to the total LER (40). Thus, if a line pattern is properly imaged, measured
60 and analysed, the obtained metrics for the LER PSD can be used to accelerate the development of
61 both high-performance photoresists and resist processing and metrology equipment, recipes and
62 protocols. However, at the moment, LER can only be measured *after* resist processing. This renders
63 it impossible to identify the LER contribution by a specific resist component or per processing step.
64 For the same reason, one cannot investigate the impact of exposure tool parameters on these
65 individual contributions. Hence, process development and control would benefit tremendously from
66 a metrology tool that can resolve (some of) these blur factors during processing and *before*
67 development. This paper shows the first experimental results for such a disruptive metrology
68 method by deploying infrared atomic force microscopy (IR-AFM) (41). In IR-AFM, an IR beam is tuned
69 to a resonance specific to an activated resist component, while a scanning probe records the locally
70 induced force field in noncontact mode. This unlocks the practical evaluation of the two geometrical
71 factors R and L in Gallatin's *R-L-S* resist metric in latent images, thereby enabling the tracking of a
72 resist's performance *between* exposure and development. We believe that in the near future, IR-
73 AFM will record chemical maps of the latent image per resist component after (during) each
74 processing step that directly reflect or even resolve these stochastics to resolve where patterning
75 resolution and uniformity are lost most.

Results

Topographical versus chemical contrast using AFM versus IR-AFM imaging

78 To perform metrology on latent patterns in cured photoresist, images were recorded by regular AFM
79 as well as with infrared-atomic force microscopy (IR-AFM) (42). To serve metrology, images shall
80 have both a sufficient signal-to-noise (S/N) and spatial resolution (21). Figure 1 shows AFM and IR-
81 AFM images of a pattern of a 500 nm wide line at 2000 nm pitch as written by electron beam
82 lithography. The 200 nm thick chemically amplified resist layer has been cured by a post-expose
83 bake but has not been developed, yielding a relatively flat sample that is easy to scan by AFM and IR-
84 AFM. As is to be expected from undeveloped resist, the S/N in the topography image by regular AFM
85 is too low to extract a clear waveform, let alone to sustain metrology (see, e.g., the left panel of
86 Figure 1). In addition, the observed pattern is hard to interpret. Resist shrinkage is inherently
87 nonlocal in effect and nonlinear, and the resulting patterns are not straightforwardly linked to the

88 actual lateral distribution of chemical changes in the resist. In IR-AFM, to enhance the chemical
89 contrast in the sample, a narrow-band IR beam is tuned to an IR absorption resonance that is specific
90 to *exposed* (and cured) resist only, while a nanometre-sized tip scans the sample with a spatial
91 resolution of at least 10-20 nm, or better (42) (43) (44) (45) (46). The IR-AFM image (centre panel of
92 Figure 1) shows a remarkable increase in S/N that has a direct link to the exposed pattern when
93 compared to regular AFM. As a result, edge detection in the IR-AFM image is straightforward (right
94 panel of Figure 1) but nearly impossible from the regular AFM image.
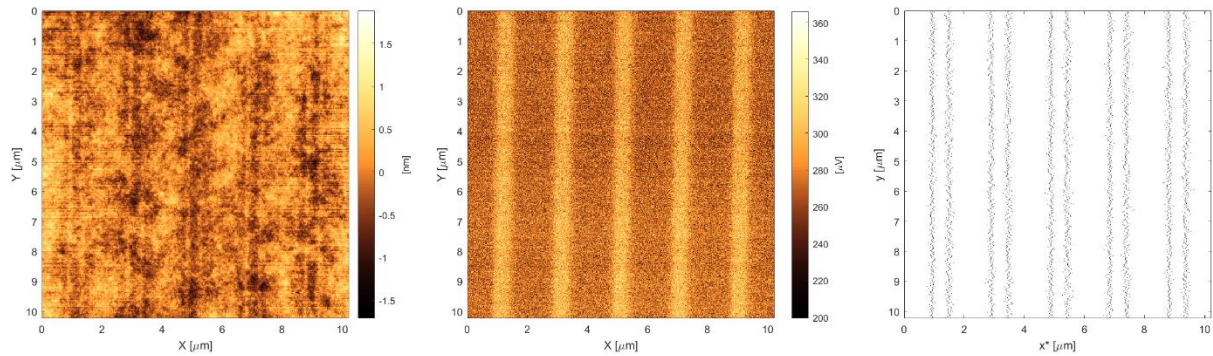

95
96

97 *Figure 1 Images of 500 nm wide lines at 2 μm pitch in exposed and baked NEB22 chemically amplified resist. The pattern*
98 *was exposed by electron-beam lithography at a dose of 40 μC cm^{-2}. The AFM image (left panel) hints at the presence of*
99 *some topography but is incapable of supporting metrology data extraction. The IR-AFM image (centre panel), recorded at*
100 *an infrared frequency of 984 cm^{-1}, yields a clear 'chemical map' of post-bake undeveloped resist. This first-of-a-kind IR-AFM*
101 *image from a latent pattern in cured resist shows similar S/N as is currently used in state-of-the-art CD-SEM. The right panel*
102 *shows line edges extracted from tilt-angle-corrected IR-AFM data. The data set has been purified by discarding isolated*
103 *edge positions that are displaced by more than 2σ from edge positions in both neighbouring lines (i.e. ~5% out of 5120*
104 *edges per image).*

105 *Table 1 Metrology data for the CD, pitch and roughness of the latent line and space patterns retrieved from purified IR-AFM*
106 *images. Roughness data are reported for direct analysis of the edge positions directly (left numbers) as well as by*
107 *integration of the PSD (right numbers).*

Dose	CD	Pitch	LER-L	LER-R	LWR	used edges
μC cm^{-2}	nm	nm	nm (1σ)	nm (1σ)	nm (1σ)	%
40	559.1	1969.3	54.1 / 54.1	63.6 / 63.7	93.4 / 93.5	94.6
80	587.3	1995.0	60.6 / 60.6	63.6 / 63.6	98.9 / 99.0	95.3

108

109 Thus, IR-AFM enables reliable LER metrology of latent patterns in resist, thereby serving the
110 development of a CAR resist that complies with the strict semiconductor industry requirements for
111 beyond sub-7 nm patterning (47).

Discussion
113 Our experimental IR-AFM data on post-bake pre-development exposed images have provided
114 reliable chemical metrology numbers for the line width as well as for the roughness of the line edges
115 and width. Currently, such a result is not achievable by conventional AFM or any other imaging
116 technique. Future IR-AFM metrology work is needed to resolve finer lines and produce chemical
117 maps of individual resist components. Although our proof of principle has been on relatively wide
118 lines, IR-AFM chemical imaging of sub-10 nm structures on similar materials has been demonstrated
119 (44) (48).

120 To better facilitate the identification of the spectral lines of interest for IR-AFM, as needed for
121 chemical mapping at the nanometre scale, it will be beneficial to conduct more detailed IR
122 spectroscopy on the bulk resist in both fresh and activated states. Having more detailed
123 spectroscopic data per resist component will pave the way for visualisation of resist chemistry per
124 processing step per component at the sub-10 nm scale. Such analysis might enable chemical
125 metrology after/during each processing step, thereby disclosing insights into resist component
126 stochastics, which has recently been recognised for its pivotal role in the resolution limit of
127 lithographic patterning (49) (36).

128 It is worthwhile to consider to what degree IR-AFM is (not) altering the resist during imaging. CD-
129 SEM, for instance, is known to cause shrinkage of the resist (21) and can also deposit a thin
130 contamination layer on (un)inspected areas. So far, IR-AFM seems harmless. After repeatedly
131 imaging the same part of the exposed resist at up to five different IR wavelengths, no alterations to
132 the topography image were observed. This observation is sustained by our (unpublished) finite
133 element modelling of local sample heating by the tip-enhanced IR intensity during the 40 ns IR pulse
134 for a wavelength tuned to an absorption peak of either SiOx or a PMMA resist sample at room
135 temperature. For the typical IR intensity, the simulated transient temperature increase during the IR
136 pulse never exceeded 50 degrees Celsius and lasted less than the IR pulse duration. A technical
137 review on IR-AFM reports a typical transient temperature rise of a few degrees Celsius on generic
138 polymer samples, which is a material class that comprises chemically amplified resists (50). Such
139 minor thermal loads are negligible when compared to either heating during exposure by the EUV
140 scanner or an effective bake to induce any chemical change during resist processing. Furthermore,
141 the IR photon energy is insufficient to directly alter or activate any resist component. Last, the
142 interaction of an AFM tip with soft matter samples is known to be potentially harmful. A recent
143 metrology benchmark study involving CD-SEM, HIM, AFM and optical metrology on developed
144 chemically amplified EUV resist showed repeated damage-free imaging of sub-50 nm contact holes
145 by AFM for a practical range of peak force settings (28). In our application of IR-AFM, a noncontact
146 mode has been selected that is known to be even gentler on the sample surface than the peak-force
147 tapping mode.

148 In summary, IR-AFM metrology on latent resist patterns has the potential to provide pivotal
149 information to develop and optimise resist composition and processing, as it may resolve the
150 development of resolution and roughness without altering the resist by charging, contamination,
151 shrinkage or heat (41).

Methods
153 A chemically amplified resist was activated by electron beam lithography and then cured by a post-
154 expose bake. To find infrared fingerprints, two sets of experiments were conducted. First, the
155 presence of any IR fingerprint was established by FTIR. Then, using the strongest line in the IR
156 fingerprint, the pattern resist was imaged by IR-AFM at sufficiently high spatial resolution for
157 metrology of pitch, line width and edge roughness. The raw data were purified by rejection of
158 statistically significant outliers in edge positions. By the purification of the raw IR-AFM images, the
159 artifacts in their power spectral density (PSD) of both LER and LWR have disappeared, and the
160 corresponding LER/LWR metrology now complies with SEMI Standard P47-0307 (51).

Sample preparation by electron beam lithography and post-exposure bake
162 A 4" silicon XX flat wafer was precleaned in an acetone bath for 5 minutes and, after rinsing in
163 isopropyl alcohol, spun dry at 2000 rpm and dried further by a 10-minute bake on a hot plate at
164 150°C. An HDMS primer was applied to the wafer shortly prior to spinning a layer of 200 nm thick

NEB 22A (Sumitomo Chemical Co.) chemically amplified e-beam resist at 6000 rpm (52). To remove the solvent, the wafer was baked at 110 °C for 2 minutes. In a Raith EBPG 5200, 4 mm wide squares and 500 nm lines at 2 micron spacing were exposed at areal doses of 40 and 80 μC cm^{-2}. The EBPG raster pixel size was set to 120 nm, and a spot size of 160 nm was selected, warranting continuous exposure of the patterns by the minor overfill of each pixel. To cure the resist, the wafer was baked at 105 °C for 2 minutes. The wafers with the cured resist were stored at room temperature in a closed box until either large-area analysis by FTIR or high-resolution imaging by IR-AFM. Figure 2 shows a cross-sectional schematic of the line pattern in the resist.
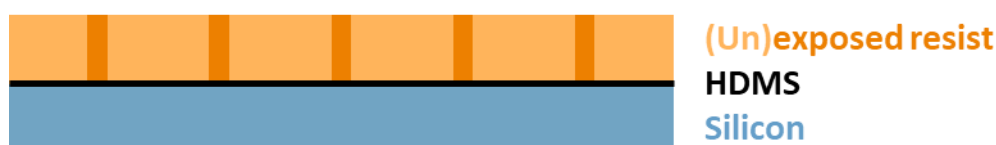

Figure 2 Schematic cross-section of the sample. A 200 nm thick NEB-22 CAR resist layer is spin coated on a silicon wafer with monolayer HDMS. The resist is exposed to a 500 nm line and spacer pattern at a 2 micron pitch using electron beam lithography with areal doses of 40 and 80 uC cm^{-2}.

Scout for chemical fingerprint of resist activation

No literature data on the IR spectra of (un)cured NEB e-beam resist could be found. Hence, in the first round of exposures, it was determined by Fourier transform infrared spectroscopy (FTIR) (53) at which IR wavelength(s) a significant detectable change was observable above what large area electron dose at the resist. A Bruker Invenio R (54) with a wide band IR DLaTGS detector was used with default settings for transmission measurements: 16 scans were made with a resolution of 2 cm^{-1} after zero padding. FTIR spectra were measured for three cases: I. a bare silicon wafer, II. a silicon wafer after coating with 150 nm NEB-22 (photoresist, before exposure), III. Idem after a cured exposure. Figure 3 shows FTIR results recorded in transmission mode for cases II and III. The difference between the spectra before and after curing exposure is relatively small because the resist layer is rather thin (150 nm) but significant. The most prominent differences occur at ~985, 1030, 1175 and 1220 cm^{-1}, with a typical width of tens of cm^{-1}. The presence of the IR peaks in the large exposed and cured areas provided experimental evidence that chemical changes in thin layers of photoresist can indeed be noticed in IR spectroscopy, albeit not yet at high spatial resolution, as is required for metrology on undeveloped resist images.

IR-AFM to resolve chemical contrast at the nanometre scale

The sample, as prepared by e-beam lithography, was examined by IR-AFM. A commercially available system, Vista One by Molecular Vista with a Block Engineering QCL tuneable mid-IR laser, was used with an NCH-Au cantilever with a tip radius of 20 nm. For topography imaging, the second cantilever mode was selected with an approximately 1 nm free air amplitude and a setpoint of 75%. The written pattern could be recognized from the topography images (figure 1) due to the well-known effect of resist shrinkage (55). This pattern allowed us to locate positions to capture IR spectra from exposed and unexposed areas of the same sample. For the IR-AFM operational conditions, we applied standard settings as suggested by the manufacturer (42). For chemical contrast imaging by IR excitation, the difference frequency between the first and second modes was used. Frequency mixing then generates a signal in the first cantilever mode. The IR laser power was set to 20%, the scan speed was 0.25 lines s^{-1} and the images were 512x512 pixels at a field of view of 10x10 microns. Figure 3 shows how large area FTIR spectra compare to single-pixel IR-AFM spectra. Generally, there is good agreement between the IR-AFM and FTIR spectra with reproduction of the same absorption peaks in both methods. At several frequencies, there are clear IR absorption differences between

207 exposed and unexposed resists. Although IR-AFM is mainly surface sensitive, it appears that there is
208 a contribution of the SiO_2 absorption peak present in the data. For imaging in IR-AFM, we selected
209 the wavelength of 984 cm^{-1} (indicated by the black line in Fig. 3), as the corresponding signal
210 enhancement is not influenced by the SiO_2 absorption peaks at approximately 1100-1200 cm^{-1} and
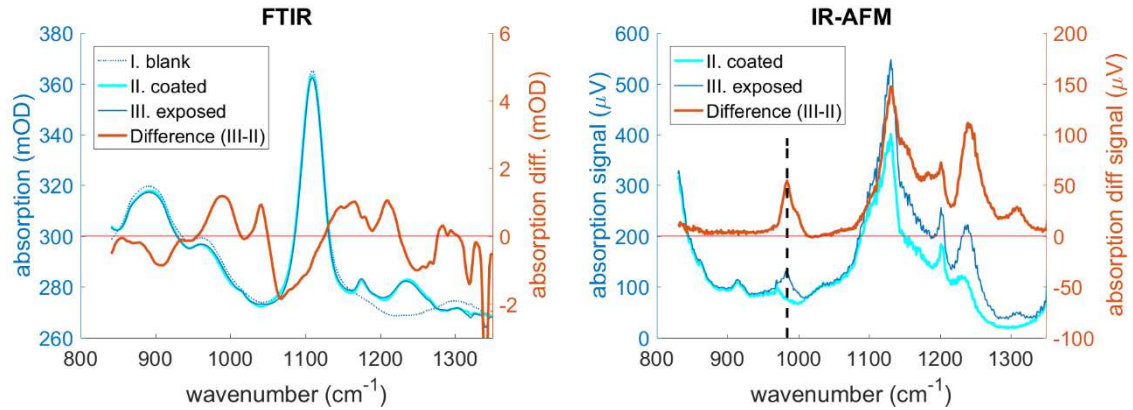211 therefore provides the best contrast.

212

213 *Figure 3 Measured infrared spectra of the (un)coated and exposed-and-cured NEB 22 resist on a Si wafer. Left: absolute (left*
214 *axis) and difference (right axis) optical density as measured by FTIR. Right: comparable spectra as measured by IR-AFM. The*
215 *IR wavelength used for imaging is depicted by the black dashed line.*

216 It is appropriate to have a short look at the comparison between topography and IR-AFM operation.
217 Although topography imaging (left panel of Figure 1) reveals hints of the printed pattern, it has poor
218 contrast, and the AFM image is not directly/easily related to the exposed pattern (55). The latter is
219 attributed to nonlocal changes in topography by resist shrinkage and/or local resist stiffness
220 changes, which fundamentally complicate accurate edge placement metrology from these data.
221 Instead, the IR-AFM image is directly related to the written pattern through the induced chemical
222 changes. Figure 4 shows the distribution of AFM and IR-AFM signal strength after classification of
223 each pixel as either "exposed" or "nonexposed" resist based on the detected edges (right panel of
224 Figure 1). Clearly, the topography contrast is only a minor fraction of the distribution widths, while
225 chemical contrast by IR-AFM is a significant fraction of the distribution widths. This confirms that IR-
226 AFM provides a reliable signal that, in addition to delivering straightforward-to-interpret images of
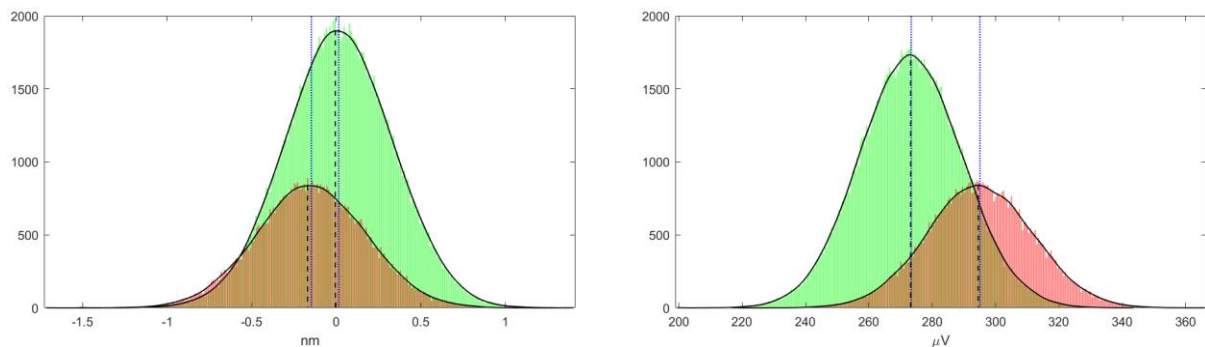227 latent resist patterns, supports quantitative analysis, e.g., LER metrology.

228

229 *Figure 4 Bottom: histograms of pixel values for exposed (green) and unexposed (red) areas. The 0,16 nm average height*
230 *difference is just a fraction of the distribution width (σ_{AFM} = 0,23 nm). The 21,7 µV difference in IR-AFM signal strength*
231 *between exposed and unexposed areas is approximately twice the distribution width (σ_{IR-AFM} = 11,7 µV).*

Waveform extraction, edge detection and data purification

233 To extract the line edge and line width roughness from the IR-AFM images, line edge positions need
234 to be evaluated over a length of at least 2 micrometres (21). To this end, after image processing to

6

purify the IR-AFM images from instrument artifacts, the average waveform was determined by fitting a raised-cosine function to each edge in the average line profile. Figure 5 shows a typical fitted waveform. The line width and centre were determined from fitted edge positions at half height (indicated by green and red dashed lines).
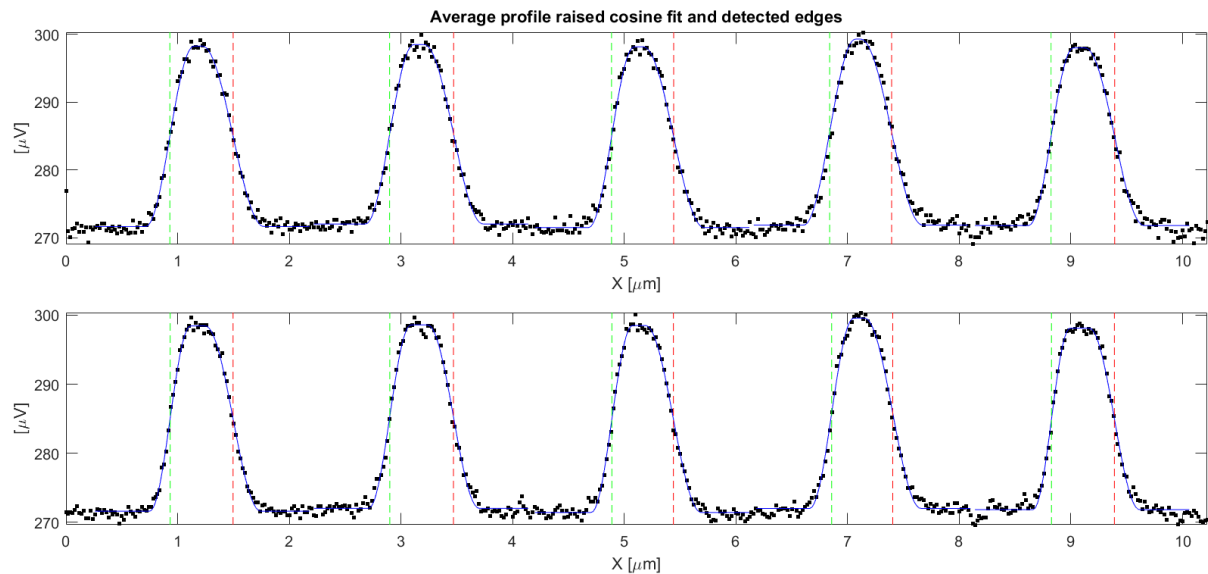

Figure 5 Average waveform (squares = data, blue line = raised cosine fit) from the IR-AFM image of Figure 1. Top: Fitted waveform used to determine the line tilt of 0.88 degrees. Bottom: final fitted waveform after correcting for line tilt. The edge positions are determined at half-height, indicated by green/red dashed lines for left/right edges.

Figure 6 shows the extracted edge positions for each image line before and after purification. The left-centre panel of Figure 6 shows all retrieved left and right edge positions relative to the line centre. The right-centre panels show all retrieved line widths. The vertical black lines indicate a 2σ deviation from the average. A first power spectral density analysis of all extracted edges (left panel of Figure 6) showed unphysical features, e.g., the LWR at lower spatial frequencies was less than the corresponding LER. Analysis of the extracted edge profiles yielded the insight that ~5% of isolated edge positions have been shifted by more than 2σ from neighbouring lines. Such shifts can be considered unphysical; hence, we purified the edge profiles by replacing these outliers by the average edge position of the neighbouring lines (right panel of Figure 6). The PSD of the purified edge positions (Figure 7) no longer shows unphysical features and can be used for chemical metrology.
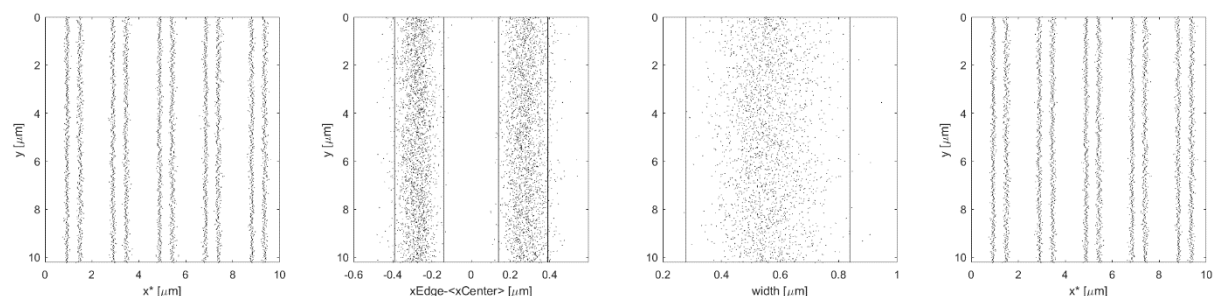

Figure 6 Detected edges before (left panel) and after purification (right). Purification involved minor tilt correction and identification of individual edge positions and/or line widths that differed by more than 2σ (indicated by the vertical straight lines in the centre panels) from both neighbouring lines. For the final LER and LWR analysis, each outlier was replaced by the average position of neighbouring edges.

Chemical metrology from line edge and width power spectral densities

Figure 7 shows a typical IR-AFM power spectral density graph calculated from the purified line profiles. The left panel also contains a {*PSD(0), ξ, H*} fit to the LER PSD after (40), following her suggestion to fix **H** = 0,5 (i.e. the theoretical value for the exponent). The right panel shows the (artefact-free) integrated PSD for the LER and LWR from the purified data.
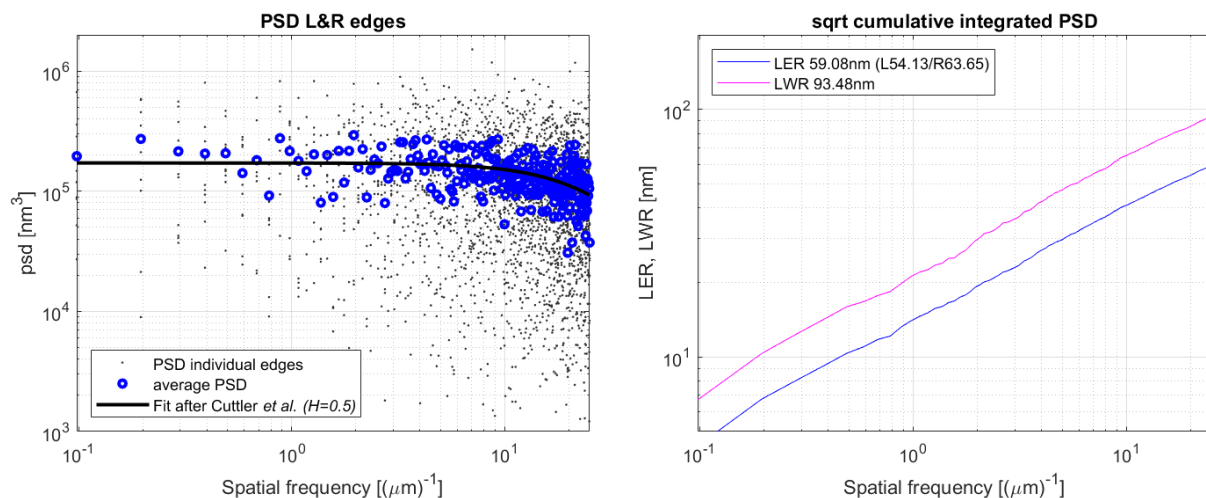

Figure 7 Power spectral density graph (right: integrated PSD) as calculated of the half-height edge positions after fitting a raised cosine waveform to each individual line of the IR-AFM image in Figure 1. Detected edges that were displaced over 2σ from direct neighbouring lines were replaced by the average edge position of the neighbouring lines.

The purified edge positions displayed in Figure 1 were analysed for LER and LWR in three independent ways, yielding a highly similar outcome, as reported in Table 1 and Table 2. First, the RMS value from the average edge position was calculated. Second, the PSD of the edge positions has been integrated after (25). Third, the PSDs of the LER and LWR from both areal doses were fitted after (40); see Table 2. For the latter, the obtained IR-AFM LER as calculated by Eq. (1) in (40) differs by a factor of 2 from the values reported in Table 1. This difference is attributed to the arbitrary choice of evaluating the PSD(f) with or without negative lateral frequencies, which obviously changes the energy per frequency.

Table 2 Fit parameters {PSD(0), ξ} as obtained from IR-AFM LER and LWR PSDs for H = 0.5, following (40). The average LER values calculated with these parameters differ by 1% from the values reported in Table 1.

Dose	PSD(0) LER	PSD(0) LWR	Ξ LER	ξ LWR
$\mu C\ cm^{-2}$	nm^3	nm^3	nm	nm
40	0,17e6	0,43e6	5,9	5,8
80	0,20e6	0,51e6	6,4	6,7

Although the values of the parameters reported in Table 1 and Table 2 in itself are not remarkable, the mere fact they could be extracted from an IR-AFM chemical image of a latent resist pattern is.

Author contributions

D. Maas partly conceived the method, outlined the experimental program, wrote most of the manuscript and, with Laurent Fillinger, purified the IR-AFM images to extract metrology data. J. van der Donck partly conceived the method and assisted in setting up the experiments. E. van Zeijl selected the NEB resist and conducted electron beam lithography exposures. E. Bloem set up,

conducted and analysed the FTIR spectroscopy of the (cured) photoresist. S. Tamer performed the IR-AFM experiments and advised on data interpretation. M. van Es and K. Maturová partly conceived the method and advised on IR-AFM experiments and data interpretation. L. Fillinger purified the IR-AFM images and extracted reliable metrology numbers. R. Willekers partly conceived the method, assisted in defining the scope of the experiments and contributed to the literature study.

Competing interests

None of the authors have competing interests.

Materials & Correspondence

Correspondence and material requests can be addressed to Diederik Maas and/or Maarten van Es.

References

1. **international roadmap committee (IRC), International Focus Teams (IFTs).** Homepage IEEE IRDS. *International Roadmap for Devices and Systems (IRDS™).* [Online] IEEE. [Cited:] https://irds.ieee.org/home/process.

2. *Nanomanufacturing: A Perspective.* **Liddle, James Alexander and Gallatin, Gregg M. .** 2016, ACS Nano, Vol. 10, p. 2995–3014.

3. *The transfer of photoresist LER through etch.* **Pawloski, Adam, et al.** sl : SPIE Press, 2006, Proc. SPIE, Vol. 6153, pp. 615318 1-11.

4. *High NA EUV: A challenge for metrology, an opportunity for atomic force microscopy.* **Moussa, A., et al.** s.l. : SPIE, 2021. Proc. SPIE. Vol. 11854, p. 1185410.

5. *The application of a Rapid Probe Microscope (RPM) for investigating 1D and 2D structures from EUV lithography.* **Humphris, A.D.L., et al.** 2020. Proc. SPIE Metrology, Inspection, and Process Control for Microlithography XXXIV . Vol. 11325, p. 113251M. ISBN 978-151063417-6.

6. *CD metrology for EUV lithography and etch.* **Johanesen, Hayley, et al.** sl : IEEE, 2015, ASMC, pp. 329-335.

7. *FinFEt scaling to 10 nm Gate Lenght.* **Yu, Bin, et al.** sl : IEEE, 2002, Digest. International Electron Devices Meeting, pp. 251-254.

8. **Levinson, Harry.** *Principles of Lithography: Third Edition.* 3. Bellingham : SPIE press, 2011. pp. 1-505.

9. **Bakshi, Vivek.** *EUV Lithography.* 2nd. Bellingham : SPIE Press Books, 2018. Vol. PM283. ISBN 9781510616783.

10. **Okoroanyanwu, Uzodinma.** *Chemistry and Lithography, Second Edition, Vol. 1: The Chemical History of Lithography.* Bellingham : SPIE Press, 2020. Vol. 1.

11. *Impact of local variability on defect-aware process windows.* **Maslow, Mark John, et al.** s.l. : Proc. SPIE, 2019. Vol. 10957, pp. 109570H 1-15.

12. *Stochastic printing failures in extreme ultraviolet lithography.* **de Bisschop, Peter.** 4, s.l. : SPIE, 2018, J. Micro/Nanolith. MEMS MOEMS, Vol. 17, pp. 041011-1-23.

322 13. *Chemical amplification resists: History and development within IBM.* **Ito, Hiroshi.** 1/2, sl : IBM,
323 1997, IBM J. Res. Develop., Vol. 41.

324 14. *Chemical Amplification Resists: Inception, Implementation in Device Manufacture, and New*
325 *Developments.* **Ito, Hiroshi.** s.l. : Wiley Periodicals, 2003, Journal of Polymer Science: Part A: Polymer
326 Chemistry, Vol. 41, pp. 3863-3970.

327 15. *Materials challenges for sub-20-nm lithography.* **Thackeray, James.** 2011, Journal of
328 Micro/Nanolithography, MEMS, and MOEMS, p. 033009.

329 16. *Pursuit of lower Critical Dimensional Uniformity in EUV resists.* **Thackeray, James, et al.** 5, 2013,
330 Journal of Photopolymer Science and Technology, Vol. 26, pp. 605 - 610.

331 17. **Thackeray, James.** Chemically amplified resists and acid amplifiers. [boekaut.] Alex Robinson en
332 Richard Lawson. *Materials and Processes for Next Generation Lithography.* sl : Elsevier, 2016, 7, pp.
333 211-222.

334 18. *Extreme ultraviolet resist materials for sub-7 nm patterning.* **Li, Li, et al.** 16, 2017, Chemical
335 Society Reviews, Vol. 46, pp. 4855-4866.

336 19. *Resist blur and line edge roughness.* **Gallatin, Gregg M.** 2005, Proc. SPIE, Vol. 5754, pp. 38-50.

337 20. *Evaluation of EUV resist materials for use at the 32 nm half-pitch node.* **Wallow, T., et al.** 2008.
338 Proc. SPIE. Vol. 6921, p. 69211F.

339 21. **Bunday, Benjamin, et al.** *Unified Advanced Critical Dimension Scanning Electron Microscope (CD–*
340 *SEM) Specification for sub-90 nm Technology (2007 Version).* Austin : International SEMATECH
341 Manufacturing Initiative, 2008. Technology Transfer . #04114595D-ENG.

342 22. *Resist Materials and Processes for Extreme Ultraviolet Lithography.* **Itani, Toshiro and Kozawa,**
343 **Takahiro.** s.l. : IOP Science, 2012, Jpn. J. Appl. Phys., Vol. 52, p. 010002.

344 23. *Sensitivity enhancement of chemically amplified EUV resists by adding acid-generating*
345 *promoters.* **Shinya , Fujii, et al.** 2017, Jpn. J. Appl. Phys., Vol. 56, pp. 06GD01-1-6.

346 24. *Fundamental study of polymer dynamic behavior in resist processing.* **Yaegashi, Hidetami.**
347 Bellingham : SPIE Proc., 2021. Vol. 11612, pp. 116120D-1-11.

348 25. *Systematic errors in the measurement of the power spectral density.* **Mack, Chris A.** 3, s.l. : SPIE,
349 2013, J. Micro/Nanolith. MEMS MOEMS, Vol. 12, pp. 033016-1-10.

350 26. *Metrology capabilities and needs for 7nm and 5nm logic nodes.* **Bunday, Benjamin, et al.** 2017.
351 Proc. SPIE Metrology, Inspection, and Process Control for Microlithography XXXI. Vol. 10145, p.
352 101450G.

353 27. *Determination of line edge roughness in low dose top-down scanning electron microscopy*
354 *images.* **Verduin, Thomas, Kruit, Pieter and Hagen, Cornelis W.** s.l. : SPIE, 2014. SPIE Proc. Vol.
355 90500, pp. 90500L-1-17.

356 28. *Sub-50 nm metrology on extreme ultra violet chemically amplified resist—A systematic*
357 *assessment.* **Maas, Diederik Jan, et al.** October 2015, Rev. Sci. Instr., Vol. 86, p. 103702.

358 29. *What is prevalent CD-SEM's role in EUV era?* **Wang, Zhigang, et al.** sl : SPIE, 2019. Proc. SPIE. Vol.
359 10959, pp. 1095914-1-10.

360   30. *Fast resist-activation dosimetry for extreme ultra-violet lithography.* **Heo, Jinsoek, Man, Xu en**
361   **Maas, Diederik.** 5, 2017, Optics Express, Vol. 25, pp. 4621-4631.

362   31. *Latent image characterization by spectroscopic reflectometry in the extreme ultraviolet.*
363   **Schröder, Sophia, et al.** 2021, Proc. SPIE, Vol. 116111, pp. M1-13.

364   32. *Influence of shot noise on CDU with DUV, EUV, and e-beam.* **Pan, Zhih-Yu , et al.** 2008. Proc. SPIE.
365   Vol. 6924, pp. 69241K 1-8.

366   33. *Roughness and variability in EUV lithography: Who is to blame? (Part 1).* **Vaglio Pret, A., et al.**
367   2013. Proc. SPIE. Vol. 8679, pp. 86792O-1-10. ISBN 978-081949461-0.

368   34. *Impact of pixel-dose optimization on pattern fidelity for helium ion beam lithography on EUV*
369   *resist.* **Kalhor, Nima, et al.** 2015. Proc. SPIE. Vol. 9425, pp. 942513-1-9.

370   35. *Improvements in resist performance towards EUV HVM.* **Yildirim, A., et al.** 2017. Proc. SPIE
371   10143. p. 101430Q.

372   36. *Multiscale simulation of extreme ultraviolet nanolithography: impact of acid–base reaction on*
373   *pattern roughness.* **Lee, Hyungwoo, et al.** sl : The Royal Society of Chemistry, 2021, J. Mater. Chem.
374   C, Vol. 9, pp. 1183-1195.

375   37. *Stochastic simulation and calibration of organometallic photoresists for extreme ultraviolet*
376   *lithography.* **Belete, Zelalem, et al.** 1, Bellingham : SPIE, 2021, J. Micro/Nanolithogr. MEMS MOEMS,
377   Vol. 20, pp. 014801-1-22.

378   38. *Photoresist and stochastic modeling.* **Hansen, S.G.** 1, 2018, J. Micro/ Nanolithogr. MEMS
379   MOEMS, Vol. 17, p. 013506.

380   39. *One metric to rule them all: new k4 definition for photoresist characterization.* **Santaclara, J.G., et**
381   **al.** 2020. Proc. SPIE. Vol. 11323, pp. 113231A-1-10.

382   40. *Pattern roughness analysis using power spectral density: application and impact in photoresist*
383   *formulation.* **Cutler, Charlotte, et al.** 2021, J. Micro/Nanopattern. Mater. Metrol., Vol. 20, pp.
384   010901 (1-18).

385   41. **Maas, Diederik Jan, et al.** *LITHOGRAPHIC PATTERNING METHOD AND SYSTEM THEREFORE.*
386   *WO2020/122724* WO, 14 12 2018.

387   42. *Nanoscale chemical imaging by photoinduced force microscopy.* **Nowak, Derek, et al.** 3, 2016,
388   Sci. Adv., Vol. 2, p. e1501571.

389   43. *Photoinduced force microscopy: A technique for hyperspectral nanochemical mapping.* **Murdick,**
390   **Ryan A., et al.** 2017, Jpn. J. Appl. Phys., Vol. 56, pp. 08LA04-1-14.

391   44. *Near-field nanoprobing using Si tip-Au nanoparticle photoinduced force microscopy with 120:1*
392   *signal-to-noise ratio, sub-6-nm resolution.* **Rajaei, Mohsen M., et al.** 20, Oct. 2018, Optics Express,
393   Vol. 26, pp. 26365 - 26376.

394   45. *New development of nanoscale spectroscopy using scanning probe microscope.* **Minn, Khant,**
395   **Birmingham, Blake en Zhang, Zhenrong.** 3, sl : AVS, 2020, J. Vac. Sci. Technol. A, Vol. 38, pp. 30801-
396   1-17.

397 46. *Nanoscale Chemical Imaging by Photo-Induced Force Microscopy: Technical Aspects and*
398 *Application to the Geosciences.* **Otter, Laura M., et al.** 1, March 2021, Geostandards and
399 Geoanalytical Research, Vol. 45, pp. 5-27.

400 47. *Novel high sensitivity EUV photoresist for sub-7 nm node.* **Nagai, Tomoki, et al.** 3, 2016, Journal
401 of Photopolymer Science and Technology, Vol. 29, pp. 475-478.

402 48. *Tip-Enhanced Infrared Imaging with Sub-10 nm Resolution and Hypersensitivity.* **Li, Jian, et al.** 5,
403 2020, J. Phys. Chem. Lett., Vol. 11, pp. 1697–1701.

404 49. *Relative importance of various stochastic terms and EUV patterning.* **Naulleau, Patrick and**
405 **Gallatin, Gregg.** 4, s.l. : SPIE, 2018, J. Micro/Nanolithogr., MEMS, MOEMS, Vol. 17, p. 041015.

406 50. *Theory of infrared nanospectroscopy by photothermal induced resonance.* **Dazzi, Alexandre,**
407 **Glotin, Francois and Carminati, Rémi.** 12, 2010, Vol. 107, pp. 124519-1-7. ISSN 00218979.

408 51. **SEMI.** *Standard P47-0307, "Test method for evaluation of line-edge roughness and linewidth*
409 *roughness.* San Jose, CA : SEMI, 2006. Standard.

410 52. *Negative chemically amplified resist characterization for direct write and SCALPEL*
411 *nanolithography.* **Ocola, L.E., et al.** 6, s.l. : Am. Vac. Soc., 1998, J. Vac. Sci. Technol., Vol. 16, pp. 3705-
412 3708.

413 53. **Griffiths, Peter R. and de Hasseth, James A.** *Fourier Transform Infrared Spectrometry.* 2nd. New
414 Jersey : Wiley-Blackwell, 2007. ISBN 978-0-471-19404-0.

415 54. **Bruker.** Invenio R. *Bruker.* [Online] 18 4 2018. https://www.bruker.com/en/products-and-
416 solutions/infrared-and-raman/ft-ir-research-spectrometers/invenio-ft-ir-spectrometer.html.

417 55. *In situ direct visualization of irradiated electron-beam patterns on unprocessed resists using*
418 *atomic force microscopy.* **Koop, H., et al.** s.l. : AVS, 2010. J.Vac. Sci. Techn. Vol. 28, pp. 802 - 805.
419 ISSN 21662746.

420